Electrochimica Acta 210 (2016) 87–95

Contents lists available at ScienceDirect

Electrochimica Acta

journal homepage: www.elsevier.com/locate/electacta

On the Model Performance of Composite CO_2 Separation Membranes

F.M.B. Marques[a,*], S.G. Patrício[a], E. Muccillo[b], R. Muccillo[b]

[a] Department of Materials and Ceramic Engineering, CICECO, University of Aveiro, Aveiro 3810-193, Portugal
[b] Center of Science and Technology of Materials, Energy and Nuclear Research Institute, S. Paulo, SP 05508-900, Brazil

ARTICLE INFO

Article history:
Received 21 March 2016
Received in revised form 18 May 2016
Accepted 20 May 2016
Available online 21 May 2016

Keywords:
CO_2 separation membranes
composite electrolytes
ambipolar conductivity
equivalent circuit
Evans-type diagram

ABSTRACT

A simple model on the performance of composite CO_2 separation membranes (ceramic oxide-ion conductor and molten alkaline carbonates) is derived from an equivalent circuit comprising two interlinked cells, using the main electrical circuit component analogs of the electrochemical characteristics of each composite phase (thermodynamic voltages and ionic resistances) and surrounding gas phase activities of species involved in the surface reactions. A newly introduced graphical solution inspired in conventional corrosion diagrams is used to benchmark, map and discuss membrane performance, including the roles of cell inner ionic transport and surface/interface reaction processes. The impact of oxide phase composition (ZrO_2, CeO_2 and Bi_2O_3- based oxides), content (40–90 vol%) and working temperature (873–973 K) on membrane performance are assessed in detail, highlighting the limits of materials currently available. Selected examples of published data on membrane performance are used to demonstrate the efficacy of the suggested diagram and to comment on permeation kinetic constraints, namely phase tortuosity.

1. Introduction

Composite electrolytes based on ceria (often Sm or Gd-doped, SDC or CGO) and eutectic mixtures of alkaline carbonates (e.g., Na and Li) possess a wide range of potential applications in fuel cells (hydrogen or direct carbon fueled), CO_2 separation membranes, steam electrolysis or even electrochemical synthesis of ammonia [1–7]. These composites combine electrolytes used in Solid Oxide Fuel Cells (SOFCs) and Molten Carbonate Fuel Cells (MCFCs). While the SOFC ceramic electrolytes are well established oxide-ion conductors, the MCFC alkaline carbonates are described either as dominant carbonate or alkaline ion conductors [8–13].

Under typical operating conditions these composite electrolytes possess multiple ionic species besides the intrinsic ones, inherent to the constituent phases. As example, the possibility of protonic conduction should not be excluded, although without consensus on the conduction mechanism due to the uncertainty on chemical species involved [14–17]. In fact, molten carbonates are a complex environment with a wide range of ionic species where the host ions (alkaline metals and carbonate) interact amongst them and with dissolved environmental species like O_2, CO_2, H_2O, H_2 [12,14,18–21]. As a consequence, unexpected species and mechanisms might be involved in surface/electrode reactions and ionic transport [3,7,12,22,23]. Most descriptions of these materials as constituents of CO_2 separation membranes consider that the dominant ionic charge carriers are oxide and carbonate ions. Here the same simplified assumption will be adopted considering that estimated ionic transport numbers of foreign ions in molten carbonates do not exceed a few percent [12].

In these composites, depending on the exact working temperature, the role of oxide-ion transport through the ceramic phase might move from dominant but small (below the carbonates eutectic temperature, often around 500 °C), to subsidiary (slightly above the carbonates melting temperature), again to relevant when reaching 700–800 °C. This apparently abnormal tendency in fact reflects the distinct temperature dependencies of the conductivities of both phases. The oxide activation energy usually shows small temperature dependence due to a shift in relevance of grain boundary versus bulk transport, maybe also in the defect association condition [24,25]. On the contrary, the carbonates move from a poorly conducting solid (with high activation energy) to a highly conducting liquid (with small activation energy), with a sharp change in conductivity when the eutectic temperature is reached [26,27].

For CO_2 separation membranes, central subject addressed in this work, the flow of carbonate ions is balanced by a counter flow of oxide ions, as such yielding a net flow of CO_2. An alternative description involving alkaline ions as relevant ionic species gives

* Corresponding author at: Department of Materials and Ceramic Engineering, CICECO, University of Aveiro, Aveiro 3810-193, Portugal.
E-mail address: fmarques@ua.pt (F.M.B. Marques).

http://dx.doi.org/10.1016/j.electacta.2016.05.141
0013-4686/

the same final result, as judiciously pointed out elsewhere [13]. The membrane operating conditions correspond to matching opposite currents inside the composite. However, charge transport by both ionic carriers shows markedly distinct temperature dependencies, as already pointed out. For proper membrane design (materials, phase percentages, working temperatures) we must be able to handle properly this situation.

The present work tries to present a simple and comprehensive model on the ideal relation between working conditions and compositions, after highlighting situations where partial conductivities match each other or where the membrane performance is governed by the slow transport of one of the species. The treatment follows a typical equivalent circuit approach, using circuit components as analogs of relevant electrochemical cells and materials characteristics, while the attempted visualization is inspired in classical corrosion (Evans-type) diagrams. Both solutions are believed to help considerably in understanding and designing key aspects determining membrane performance. With the simple guide on ideal relations between phase composition and membrane operating temperature, promising ceramic materials and oxide content for target applications can be easily screened. Lastly, we map and comment the results obtained so far with CO_2 separation membranes with respect to what might be described as ideal performance.

2. Comprehensive electr(ochem)ical model of membrane performance

Modelling of composite CO_2 separation membranes deserved some attention in recent years in order to explain their performance or to circumvent limiting factors. One first attempt addressed the performance of these membranes assuming that the composite partial conductivities (ionic and electronic) were independent of the gas phase composition [28]. This base model was extended to account for microstructural features with impact on the required mixed ionic transport. This transport is mostly determined by the ionic conductivity of each pure phase and their volume fraction but also influenced by parameters accounting for the microstructural characteristics of each phase like tortuosity. The latter aspect takes into consideration the effective ionic transport pathway length, larger than the actual composite cell thickness [29,30].

More recently, another model was used to describe the composite membranes, taking now into consideration the dependence of the electronic conductivity on the activities of relevant gas species [13]. All these models rely on the consideration of two electrolytes (molten carbonates and solid oxide) arranged in parallel (Fig. 1a) as in actual microstructures of composite membranes where both phases percolate throughout the composite cell thickness, providing parallel pathways for ionic transport.

Interestingly, although both models indeed rely on a similar conceptual equivalent circuit, no attempt was yet made to discuss the membrane performance using entirely the equivalent circuit analogy. This procedure is in line with the old (but still sensible) suggestion by Hoar and Price [31] to address in an alternative (simpler) manner the treatment of the tarnishing behavior of metals, firstly introduced by Wagner [32]. This equivalent circuit analogy was further developed throughout the years in the field of solid state ionics aiming at the consideration of distinct realities involving mixed ionic and electronic conduction [33,34], and will be hereby adapted to the present situation.

2.1. Equivalent circuit, circuit elements and analysis

Fig. 1a shows a global scheme of the adopted equivalent circuit. In practice we have two cells (MC/molten carbonates – upper cell, and SO/solid oxide – lower cell) with ionic and electronic branches accounting for the possibility of both types of charge transport. Ionic resistors (R_j, with j = MC or SO), electronic resistors ($R_{j,e}$) and cell thermodynamic voltages ($V_{o,j}$) are the required circuit elements. I_j and $I_{j,e}$ are the cell inner ionic and electronic currents, respectively. At the surface of each cell (feed and permeate sides) the chemical activities of the gas species (CO_2, O_2) involved in the cell reactions are responsible for the thermodynamic voltages, as detailed later.

When adopting the equivalent circuit analogy we can choose between a simple approach where circuit elements (resistors), related to the materials electrical properties (ionic and electronic), are averaged and constant within the entire range of working conditions (only temperature dependent) or a more accurate

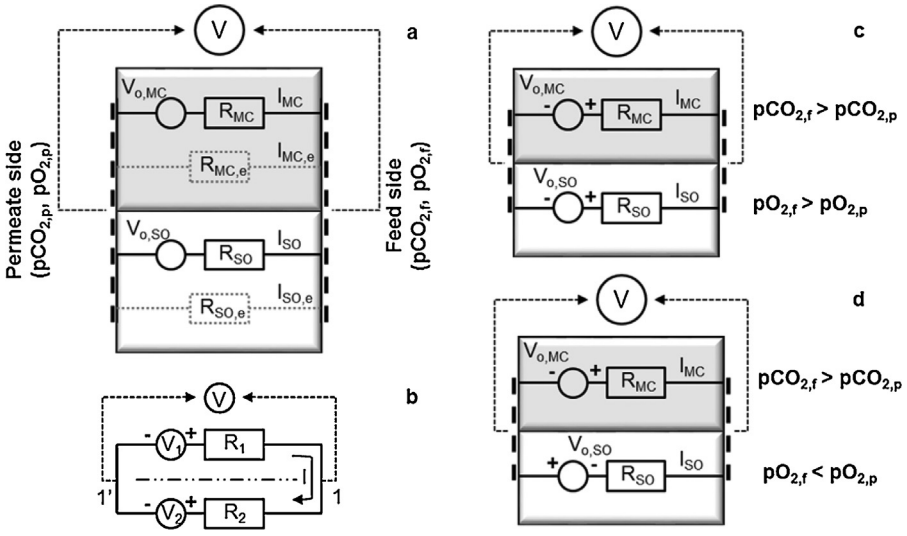

Fig. 1. (a) General equivalent circuit for composite membranes with solid oxide (SO) and molten carbonate (MC) cells in parallel. Circuit elements: thermodynamic cell voltages $V_{o,j}$ and ionic and electronic resistances, R_j and $R_{j,e}$, respectively (with j = MC or SO). Ionic and electronic currents (I_j and $I_{j,e}$, respectively) also shown; (b) simplified circuit used to illustrate the application of the Kirchhoff's voltage law (see text for details); (c) and (d) simplified circuits showing the relations between the polarity of cell voltages and carbon dioxide and oxygen partial pressure boundary conditions.

methodology where the cell is analyzed as if of differential thickness, allowing for the consideration of the dependence of electrical conductivity on surrounding chemical activities [33,34]. The simpler approach will be adopted here. We will also consider that the outer surfaces of each membrane correspond to equipotential surfaces [13], situation depicted in Fig. 1a using a dashed line as if corresponding to an electronic conductive layer. In fact this condition is used in typical cell voltage measurements performed under distinct gas activity gradients [12]. Lastly, for the remaining discussion we will neglect the electronic conductivity, which explains the utilization of dotted lines for the electronic branches in Fig. 1a. By definition electrolytes are materials with negligible electronic conductivity with respect to their ionic conductivity. Anyhow, the detailed critical assessment of these decisions can be found in the section on final remarks.

A simplified electrical circuit derived from Fig. 1a and taking into account these assumptions is shown in Fig. 1b. The rationale for the adopted cell polarity will appear later in this discussion. Since there is no current flowing outside the electrochemical cells (no outside circuit), the formal cell parallel arrangement in fact originates a series type association. From elementary circuit analysis, using the Kirchhoff's voltage law, the sum of all voltages around the circuit must be zero. With the current direction shown in Fig. 1b this means that $-V_1 + I.R_1 + I.R_2 + V_2 = 0$ [35]. Furthermore, since points 1 and 1′ are shared by both sub circuits, the voltage drop between these points must be the same irrespective of the branch. In practice this means that one cell is short-circuiting the other as in real membranes.

2.2. Membrane operating conditions

Arrived here, the origin and polarity of thermodynamic voltages must be addressed in further detail. The following (half-cell) reactions (reduction in the forward direction, oxidation in the reverse direction) can be assumed for the molten carbonates and solid oxide, respectively:

$$2\ CO_2 + O_2 + 4\,e^- \leftrightarrows 2\ CO_3^{=} \quad (1)$$

$$O_2 + 4\,e^- \leftrightarrows 2\ O^{=} \quad (2)$$

At the membrane feed side forward reaction (1) is combined with reversed reaction (2) ($2\ CO_2 + 2\ O^{=} \rightarrow 2\ CO_3^{=}$), situation depicted in Fig. 2a. At the membrane permeate side we have the opposite combination ($2\ CO_3^{=} \rightarrow 2\ CO_2 + 2\ O^{=}$). In this manner we have no net flow of electrons or molecular oxygen. If the membrane is indeed covered with an electrode (e.g., see [12]), we can envisage complementary delocalized reactions involving charge transfer, with the same overall result (Fig. 2b). Scheme 2b can concur with Scheme 2a in the presence of electrodes on each membrane surface but this is not true in the absence of electronic transport where Scheme 2a is the only valid global mechanism for the assumed relevant charge carriers.

Since the oxide and the carbonates possess distinct electrochemical properties, they also experience distinct thermodynamic voltages ($V_{o,j}$), driven by the chemical composition of the surrounding atmospheres and cell reactions just presented ($V_{o,j} = -\Delta G_j / n_j F$, with ΔG_j the corresponding Gibbs free energy change, n_j the number of electrons involved in each cell reaction and F the Faraday constant).

In the usual membrane operating mode we are in the presence of gas concentration cells where the relevant species are CO_2 and O_2 at both sides of the membrane (see reactions (1) and (2)). Consequently, with the activities of these species determining the thermodynamic voltages experienced by each cell, we can express them as:

$$V_{o,MC} = \frac{RT}{2F}.\ln\frac{pCO_{2,f}}{pCO_{2,p}} + \frac{RT}{4F}.\ln\frac{pO_{2,f}}{pCO_{2,p}} \quad (3)$$

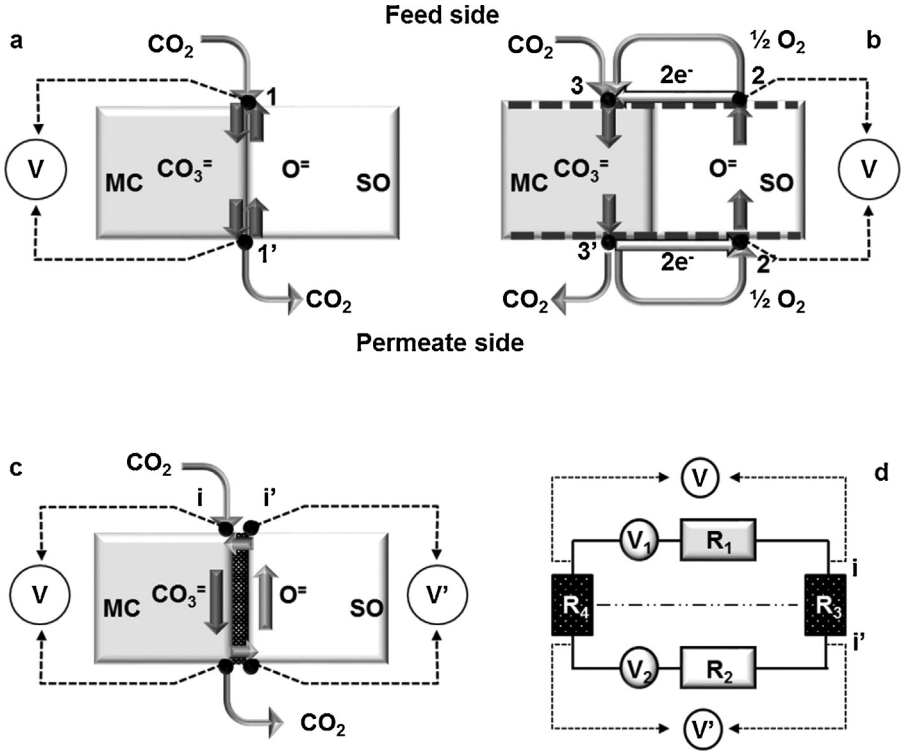

Fig. 2. Feed and permeate side possible surface reactions without (a) and with (b) charge transfer. 1-1′, 2-2′ and 3-3′ correspond to distinct typical pairs of triple phase boundary points where these reactions must occur. In (c) and (d) the impact of a slow transfer of oxide ions due to the formation of an insulating layer with resistance R_3/R_4 in the feed/permeate sides, responsible for a local voltage drop (e.g., between i and i').

$$V_{o,SO} = \frac{RT}{4F}.\ln\frac{pO_{2,f}}{pO_{2,p}} \quad (4)$$

assuming equilibrium in the surface reactions. In these equations pO_2 and pCO_2 correspond to the partial pressures of oxygen and carbon dioxide in the gas phase (used here instead of the corresponding activities) while the subscripts f and p refer to the distinct membrane boundary conditions (feed and permeate sides, respectively); R and T have their usual meanings.

We have two interlinked electrochemical cells with the same or opposite polarity, depending on the exact membrane boundary conditions (Fig. 1c and d). However, irrespective of the oxygen activity gradient across both cells, the combined result of both thermodynamic voltages will be always the same. In fact, the net thermodynamic voltage will be the difference (opposed polarity in series, Fig. 1c) or the sum (same polarity in series, Fig. 1d) of individual cell voltages, cancelling in this manner the variable sign of $V_{o,SO}$.

As a study case, we will stick now to a flue gas resulting from combustion of a fossil fuel, as such rich in CO_2 (e.g., >10 vol%). A modest O_2 content of only a few percent (e.g., 1–2%) would be typical of a slight oxygen excess with respect to stoichiometric combustion requirements, condition often used to ensure full fuel conversion and high energy efficiency. These boundary conditions apply to the membrane feed side. In the membrane permeate side we would expect a low partial pressure of both gases due to light vacuum (Fig. 1c). The corresponding simplified circuit was already depicted in Fig. 1b.

In these circumstances, in the absence of any electronic transport across the membrane or via an external load resistance connecting the membrane surfaces, we can only sustain a steady flow of CO_2 (as carbonate ions) from the feed side to the permeate side (forward reaction (1)) if we have a counter flow of oxide ions via the solid electrolyte (reaction (2) backwards), to ensure a balanced charge flow inside the membrane (nil total current). But the reversed direction (2) would be against the spontaneous direction if the solid oxide phase was alone, with the pO_2 in the feed side higher than in the permeate side, as assumed. So, if not spontaneous, reaction (2) must be driven backwards by the opposite (higher) thermodynamic voltage of the molten carbonates. This means that the molten carbonates concentration cell is running in galvanic mode (spontaneous reaction) while the solid oxide concentration cell is forced to run in electrolytic mode (endergonic reaction).

This reasoning can be further developed using standard relations for galvanic and electrolytic cells. Assuming dominant ohmic losses in both cells, the corresponding individual cell voltages (V_{MC} and V_{SO}) should follow:

$$V_{MC} = V_{o,MC} - |I_{MC}|.R_{MC} \quad (5)$$

$$V_{SO} = V_{o,SO} + |I_{SO}|.R_{SO} \quad (6)$$

Also, considering the equivalent circuits shown in Fig. 1 and inherent considerations, the working voltages and currents (V and I) in both cells must obey:

$$V = V_{MC} = V_{SO} \quad (7)$$

$$I = |I_{MC}| = |I_{SO}| \quad (8)$$

Combining relations (5) through (8) we obtain $-V_{o,MC} + I.R_{MC} + V_{o,SO} + I.R_{SO} = 0$, exactly the condition previously presented for the circuit shown in Fig. 1b, imposed by the Kirchhoff's voltage law. In fact, we should recall here that under the assumption of equipotential cell surfaces the voltage across both cells must be the same (points 2 and 3 versus 2′ and 3′ in Fig. 2b). Even without the assumption of perfect equipotential surfaces, the electric potential in the feed side contact point 1 must be the same for both cells (Fig. 1b and a). The same holds for point 1′ in the permeate side (also Fig. 1b and a). In short, the thermodynamic voltages of both cells are distinct (equations (3) and (4)) but the working voltages are the same (equation (7)) since they meet at shared contact points. Deviation from this condition is only possible if the surface/interface reactions are not in equilibrium, as suggested in Fig. 2c and d, situation discussed later in this work.

If we combine now equations (3) through (8), we can express the operating current as a function of the membrane boundary conditions and the partial solid oxide and molten carbonates conductivities ($\sigma_{p,j}$) within the composite membrane:

$$I = \frac{RT}{2F(R_{MC}+R_{SO})}\ln\left(\frac{pCO_{2,f}}{pCO_{2,p}}\right) = \frac{SRT.\sigma_{p,MC}.\sigma_{p,SO}}{2Fd.(\sigma_{p,MC}+\sigma_{p,SO})}\ln\left(\frac{pCO_{2,f}}{pCO_{2,p}}\right) \quad (9)$$

Here the adopted relation between resistance (R) and conductivity (σ) for each phase was the standard one ($R = d/\sigma.S$, with S and d being the membrane surface area and thickness, respectively).

From eq. (9) we can immediately recognize that maximum performance is obtained when the sum $R_{MC} + R_{SO}$ is minimized. If one of the resistances is larger than the other, the former becomes rate determining. In eq. (9), the term $\sigma_{p,SO}.\sigma_{p,MC}/(\sigma_{p,SO} + \sigma_{p,MC})$ is the ambipolar conductivity of the composite, central for the optimization of membrane performance. This is strongly dependent on actual phase constituents, also influenced by their corresponding volume fractions and working temperature, as discussed in the following text.

The inner membrane current can be expressed as a function of the volume fraction of each phase and their nominal conductivities as dense and pure phases:

$$I = \frac{SRT.(1-\chi)\sigma_{MC}.\chi\sigma_{SO}}{2Fd.[(1-\chi)\sigma_{MC}+\chi\sigma_{SO}]}.\ln\left(\frac{pCO_{2,f}}{pCO_{2,p}}\right) \quad (10)$$

with χ being the solid oxide volume fraction. To reach this result the assumed partial conductivity within the membrane is a direct function of the pure phase conductivity weighted by the corresponding volume fraction (e.g., $\sigma_{p,SO} = \chi.\sigma_{SO}$).

Since the basic assumptions are the same equation (10) is in all aspects equivalent to the result of previous modelling [28], after conversion of currents (I) into CO_2 permeation fluxes ($J = I/2FS$). The overall simplicity of the entire approach just presented can be easily understood from comparison with previous work. The tortuosity effect on the conductivity of each phase can also be considered, in line with previous work [29,30], but this aspect will be considered only in the discussion of published data on membrane performance.

Combination of equations (3) through (8) is also possible to obtain the voltage across the membrane. This is the usual procedure to determine the average ionic transport numbers for distinct species [12]. Light mathematical handling of these relations yields:

$$V = t_{MC}\left[\frac{RT}{2F}.\ln\frac{pCO_{2,f}}{pCO_{2,p}} + \frac{RT}{4F}.\ln\frac{pO_{2,f}}{pO_{2,p}}\right] + t_{SO}\left[\frac{RT}{4F}.\ln\frac{pO_{2,f}}{pO_{2,p}}\right] \quad (11)$$

In equation (11) t_{MC} and t_{SO} are the average ionic transport numbers of the relevant charge carriers in the distinct phases, which are often expressed as a function of the partial ionic

conductivities or ionic resistances:

$$t_{MC} = \frac{\sigma_{p,MC}}{\sigma_{p,MC}+\sigma_{p,SO}} = \frac{R_{SO}}{R_{MC}+R_{SO}} \quad (12)$$

$$t_{SO} = \frac{\sigma_{p,SO}}{\sigma_{p,MC}+\sigma_{p,SO}} = \frac{R_{MC}}{R_{MC}+R_{SO}} \quad (13)$$

3. Discussion

3.1. A schematic diagram of membrane performance

In a composite membrane we have two reversible reactions interlinked and, as already mentioned, the membrane operating condition in the feed side corresponds to equal rates of forward reaction (1) and backward reaction (2). These reaction rates can be conveniently described as currents. The resemblance between the membrane operating conditions and corrosion problems where anodic and cathodic reaction rates must coincide is obvious. Arrived here, it seems worth to exploit this resemblance from a pictorial perspective as in Fig. 3a and b, introducing a diagram similar to Evans-type corrosion diagrams, after suitable adjustments. The newly suggested diagram shows the dependence of the two cell voltages on the membrane internal currents. As schemes, in Fig. 3a and b currents were normalized against the highest absolute value considered, corresponding to point A, here used as reference.

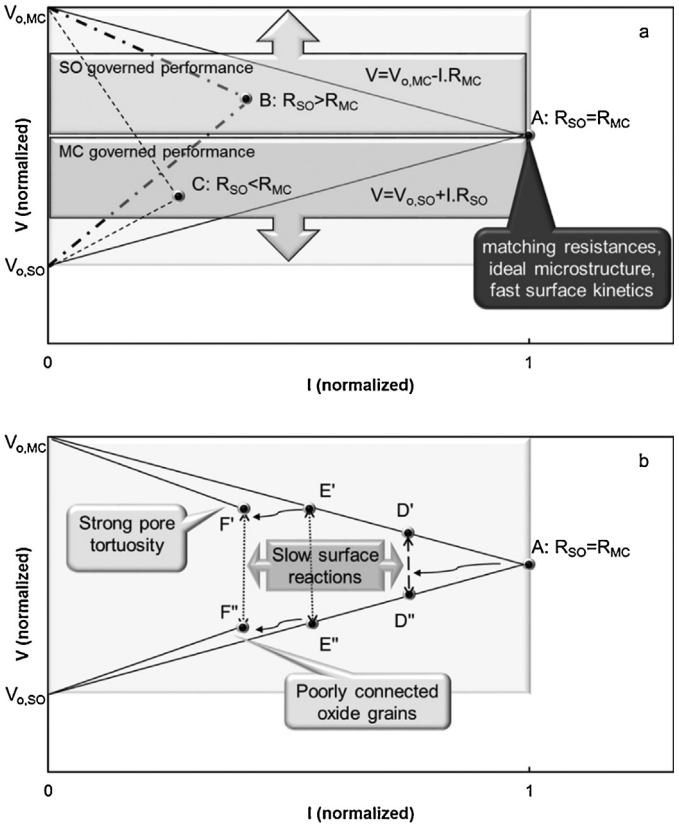

Fig. 3. Schematic diagrams highlighting several possible operating conditions of composite CO_2 separation membranes. The starting points ($V_{o,MC}$ and $V_{o,SO}$) are the distinct cell thermodynamic voltages. The slopes of V (voltage) versus I (current) lines are related to the distinct cell ionic resistances, R_{MC} and R_{SO}. In (a), points A, B and C correspond to distinct ratios between ionic resistances. In (b), the impact of slow surface/interface processes and poor microstructures is introduced with the position of the couple D'/D" versus A, and of F'/F" versus E'/E", respectively. See main text for further details.

Based on the assumed membrane boundary conditions the voltage described by equation (3) is larger than the voltage estimated by equation (4), which explains the relative positions of $V_{o,MC}$ and $V_{o,SO}$ in Fig. 3a. Thus, the starting point of each line in the diagram corresponds simply to the thermodynamic voltage that would be experienced independently by each phase if exposed to the mentioned boundary conditions (open circuit condition, no internal current, I = 0). This thermodynamic voltage window (gap between $V_{o,MC}$ and $V_{o,SO}$) will be used to drive ohmic (ionic transport across the membrane) and non-ohmic processes (surface/interface processes) involved in the membrane operation.

For the molten carbonates, the larger the current the lower the cell voltage (equation (5)). For the solid electrolyte, a voltage larger than the cell open circuit voltage is needed (equation (6)). Equations shown in Fig. 3a recall the relation between slopes of lines and ionic resistances of membrane phases. Depending on the relative magnitudes of ionic resistances, lines departing from $V_{o,MC}$ and $V_{o,SO}$ meet at points like A, B or C. Each point corresponds to a current/condition where the rates of the cathodic half-reaction in (1) and the anodic half-reaction in (2) are the same.

In general, a composite membrane can operate roughly in any point within the shadowed area in Fig. 3a and b. Since the actual composite membrane working condition corresponds to identical currents through both phases, the exact operating condition will depend on the exact values of both cell resistances. If one of the resistances is higher than the other, the membrane efficiency will be limited by the most resistive component (see eq. (9)). Point A, used as illustrative reference, corresponds to a condition where both resistances are identical.

Unbalanced ionic resistances are also shown in Fig. 3a (points B and C). Point B corresponds to a constrained membrane performance where the membrane permeation rate is governed by the high solid oxide resistance. Such conditions are expected for most combinations of available oxides and salt mixtures, given their electrical properties. Point C corresponds to a constrained membrane performance where the membrane permeation rate is governed by a high molten carbonate resistance. This is an unusual situation for state of the art materials, and is considered here just as example. The working conditions can change changing the base materials, using inadequate microstructures (namely with strong phase tortuosity), or even decreasing the working temperatures. In the following diagrams all these aspects will be further detailed.

In Fig. 3b the combined impact of slow surface kinetics and poor microstructures is introduced in a schematic manner, starting again from point A as reference. Slow surface/interface steps of any type will displace the working condition from point A to the left in the diagram, as in the couple D'/D". A typical example would be the formation of an insulating layer between both composite phases due to chemical interaction. The corresponding scheme is presented in Fig. 2c. R_3 and R_4 in Fig. 2d reflect the newly formed resistances that might be similar or distinct depending on the characteristics of the layer in the feed and permeate sides. This situation can originate a voltage drop with magnitude corresponding to the length of the vertical dashed line between D' and D". This decreases the available voltage to drive ionic transport, decreasing the net overall current.

Poor microstructures resulting in constricted pathways for ionic transport in both phases will be responsible for enhanced (absolute) slopes of the lines describing the operation mode of both sub-cells, as pointed out when we move from couple E'/E" to couple F'/F", again with decreasing overall net current.

One way to influence membrane efficiency is to act on the thermodynamic voltage window between $V_{o,MC}$ and $V_{o,SO}$. For the same resistances, if values $V_{o,MC}$ and $V_{o,SO}$ move away from each other, the working currents also move to the right. This solution is obviously constrained since the operating conditions are dictated by the composition of the flue gas available.

3.2. Predictable roles of composition and temperature on membrane performance

When the content and electrical properties of each phase are known, the definition of a target membrane performance is quite easy, using equation (10). In this equation all microstructural effects besides phase content were neglected. Thus, any experimental results on the actual electrical characteristics (resistance) of the distinct phases in a real composite or on membrane performance (effective CO_2 separation rates) can be plotted in the previous diagrams against the target performance obtained from equation (10). This shows how versatile these diagrams are to map and benchmark actual membrane performance, since target values can be easily estimated from literature data and actual values obtained from a variety of measurements.

Benchmarking membrane performance with respect to composition and temperature is exploited in Fig. 4, including three main sets of calculations on target membrane performance (I_{cell}) at constant temperature (923 K), using one same salt mixture (NLC, the eutectic composition in the system Na_2CO_3 and Li_2CO_3), distinct oxides and variable oxide contents (from 40 to 90 vol%, 10 vol% increments, black filled symbols correspond to an oxide content of 60 vol%.). Reference data and sources for the electrical properties of CGO (Gd-doped ceria), YSZ (yttria stabilized zirconia) or BYS (Y and Sm co-doped Bi_2O_3) and NLC, are shown in Table 1. The assumed CO_2 and O_2 partial pressure ratios in the feed and permeate sides were $\ln(pCO_{2,f}/pCO_{2,p}) = 4$ and $\ln(pO_{2,f}/pO_{2,p}) = 6$, close to sets of values found in published data [38]. All calculations assumed the same membrane dimensions (0.5 cm diameter and 0.1 cm thick).

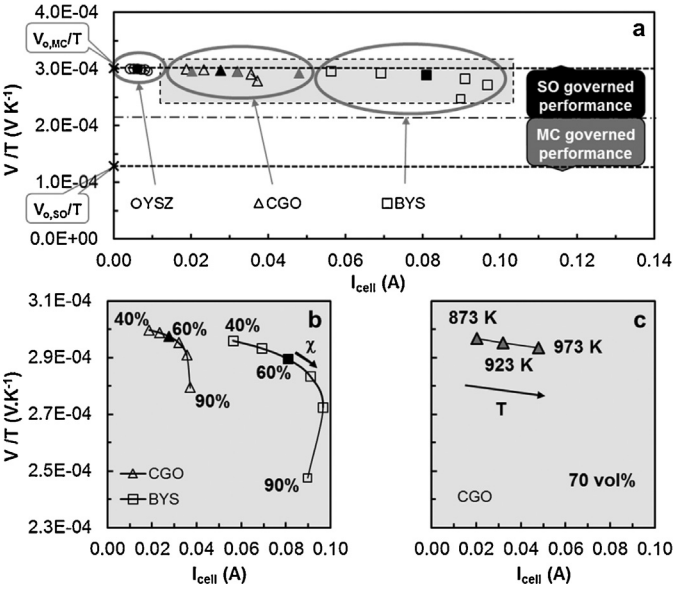

Fig. 4. (a) Diagram showing the predictable influence of the oxide phase nature (YSZ, CGO, BYS), content (χ) and working temperature (T) on a composite membrane ideal permeation current (I_{cell}), for several well-known oxide-ion conductors (data sources mentioned in Table 1). In (b) and (c) detailed views of the shadowed area in (a) highlighting the roles of oxide phase content (χ, as vol%) and temperature (T, in K), respectively. See text for further details.

Table 1
Electrical properties of selected materials (used in Figs. 4 and 5).

Acronym	E_a/kJ mol^{-1}	σ_{923K}/S cm^{-1}	Ref.
NLC	16.9	2.29	[27]
CGO	54.6	3.79×10^{-2}	[25]
YSZ	71.2	8.06×10^{-3}	[36]
BYS	90.4*	1.16×10^{-1}	[37]
SDC	62.8	3.10×10^{-2}	[38]

* Average value estimated in the 773 to 973 K range.

Besides compositional effects, a complementary set of grey filled symbols describes the predictable impact of working temperature on the performance of a 70 vol% CGO-based membrane (50 K increments starting at 873 K). Voltages (vertical axis) were divided by the absolute temperature to obtain a common voltage window, for an easier visualization of all results in one single diagram.

One first reading can be obtained from the global positions of all sets of points in Fig. 4a, grouped within three closed grey lines. Permeation currents should increase enormously from YSZ (circles) to CGO (triangles) and again to BYS (squares) based membranes, following the known tendency for oxide-ion conductivity in these oxides. Furthermore, all estimated values line up along an almost horizontal line starting at $V_{o,MC}/T$. This is not surprising since the ionic conductivity of molten carbonates is much higher than for standard ceramic electrolytes. This simply means that membrane performance in all these examples is governed by oxide-ion transport.

The obvious solution to facilitate oxide-ion transport within the membrane is to increase the ceramic phase content in the composite. The impact of oxide phase content on membrane performance is shown in Fig. 4b, a detailed view of the area within the dashed line in Fig. 4a (only CGO and BYS-based membranes). Since the lower ceramic phase content used in these calculations was 40 vol%, there is clearly room for some improvement in membrane performance increasing the amount of ceramic in the composite. In fact, the estimated maximum membrane performance is reached for the condition of maximum ambipolar conductivity at each temperature:

$$\chi_{SO} = \frac{\sigma_{MC} - \sqrt{\sigma_{MC} \cdot \sigma_{SO}}}{\sigma_{MC} - \sigma_{SO}} \qquad (14)$$

and corresponds to extremely high ceramic phase content (≥80 vol %) for all these oxides. This result can be easily obtained equating to zero the derivative of the ambipolar conductivity with respect to the oxide phase content. However, comparison of performance enhancements due to increasing oxide phase content or changing the ceramic phase shows that major improvements must rely on distinct solid oxides with respect to the state of the art materials. Thinner membranes might be equally effective, considering equation (10).

Precaution is needed on the effectiveness of extremely high ceramic contents. We must realize that although with one phase in the liquid state, easily wetting and spreading through open holes of a ceramic backbone, when we reach oxide contents close to or in excess of 90 vol% the likelihood of trapped or poorly percolating molten carbonate regions, without actual contribution to the ionic transport, is high. This means that other microstructural limits must be considered (tortuosity, loss of percolation, etc.), situation here just pointed out.

Looking now at temperature effects (see sequence of grey symbols in Fig. 4a, situation detailed in Fig. 4c) it seems obvious that changing the operating temperature has some efficacy with respect to membrane performance. The (70 vol%) CGO-based example exploited in these calculations, showed an overall

performance enhancement of about 3× between 873 and 973 K. However, this situation has obvious operational constraints, preventing entire freedom in the definition of a working temperature.

3.3. Detailed analysis of membrane performance

In Fig. 5 a final complementary exercise is introduced to map and comment actual (BYS, SDC and CGO-based) membrane performance at 923 K, using the newly introduced diagrams. Totally comparable sets of data are hardly found since distinct authors use different membrane characteristics (compositions and dimensions), besides distinct gas compositions. As such, data handling was only possible under certain assumptions, detailed below. Membrane performance targets were estimated using equation (10), reported cell dimensions and membrane phase composition (Table 2), besides the electrical properties of pure and dense phases (Table 1). Since in the selected examples no O_2 was added to any gas stream, the assumed oxygen partial pressure gradient across the cells was zero ($V_{o,SO} = 0$). Furthermore, information on the CO_2 content is often available only for the feed side. As such, the corresponding content in the permeate side was presumed as the result of perfect mixing within the inert carrier gas (all CO_2 permeating across the membrane perfectly diluted in the carrier).

The small inset in Fig. 5a shows a global map of BYS, SDC and CGO-based membrane performance while a detailed analysis of the information on the CGO-based membrane is shown in the larger diagram. In Fig. 5b only the BYS-based membrane is considered. A deeper analysis of the performance of the SDC-based membrane was discarded given the similarity with respect to the CGO-based membrane, where more information is also available. This includes the electrical characterization of numerous porous CGO substrates [39] and of freshly prepared porous skeletons and CGO-based membranes (Fig. 6), similar to those used in permeation experiments [23]. Details on processing and characterization of these materials can be found elsewhere and will be skipped here for being irrelevant for the present discussion [23].

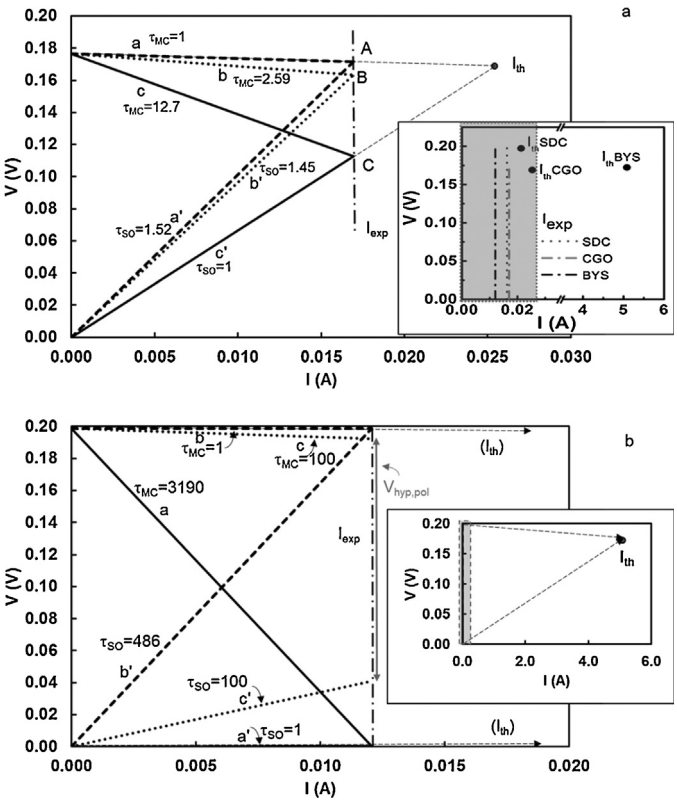

Fig. 5. Diagrams on membrane performance, based on published data: (a) Inset with global mapping of actual (vertical lines, I_{exp}) and ideal permeation currents (points, I_{th}) for BYS, SDC and CGO-based membranes. In the main diagram an expanded image of the shadowed area showing distinct tortuosity values matching the CGO-based membrane performance; (b) The main diagram for the BYS-based membrane details the shadowed area in the inner figure. The large mismatch between I_{exp} and I_{th} is only possible assuming exorbitant tortuosity values (> 100) or sluggish surface kinetics (large $V_{hyp,pol}$). See Tables 1, 2 and main text for further details.

Since all these membranes possess distinct dimensions and were exposed to slightly distinct atmospheres (Table 2), absolute current values are of modest meaning unlike relative values for each membrane (I_{exp} versus I_{th}). In all cases actual performance is below benchmarks. One obvious explanation is that the benchmarking exercise involved data from distinct sources, not necessarily coinciding with the actual properties of materials used in membrane fabrication. However, the most likely reason is that benchmarks neglect microstructural effects and surface reaction kinetics as discussed below.

Tortuosity (τ_j), as suggested elsewhere, describes the relation between the ideal partial conductivity of phase j and the experimental conductivity, σ_{exp} ($\tau_j = \sigma_{p,j}/\sigma_{exp} = \chi_j.\sigma_j/\sigma_{exp}$) [29,30]. Since the constraint is the actual permeation current, distinct levels of tortuosity can be combined to reach a given I_{exp}, as shown in Fig. 5a for three main couples of lines (aa', bb' and cc'). Lines a and a' correspond to a limiting condition where tortuosity effects are only present in the oxide phase ($\tau_{SO} = 1.52$). In lines c and c' we have the other limiting case where tortuosity effects are only present in the molten carbonates ($\tau_{MC} = 12.7$).

According to published data on the conductivity of porous CGO substrates a tortuosity of 1.52 can be obtained for a densification of 75.9%. For CGO 69.9% dense this number increases to 2.44 [39]. However, while distinct microstructures might originate distinct tortuosity values, the order of magnitude of this limiting case seems reasonable. In fact, own conductivity measurements of a twin porous CGO skeleton at 923 K (Fig. 6) yielded a value of 1.14×10^{-2} S cm^{-1}, close to the value of 1.32×10^{-2} S cm^{-1} reported in the literature for a similar densification [39].

The upper limit for the tortuosity of the molten carbonate phase (12.7) seems to be clearly an exaggerated value. In fact, the total conductivity of a similar CGO-based membrane at 923 K was about 8.48×10^{-2} S cm^{-1} (Fig. 6). After deduction of the assumed oxide partial conductivity an upper tortuosity value in the order of 7.80 can be guessed for the molten carbonates. Looking again at literature data, estimated tortuosity values for the molten carbonate phase were all below 2–3 [29,30]. This latter range of values seems quite sensible since we are dealing with ionic motion in a liquid, as such hardly more constrained than expected for the solid phase with grain boundaries besides other microstructural constraints.

Based on these considerations, an exercise was drafted in Fig. 5a for the CGO-based membrane, corresponding to lines b and b', meeting in point B. Along with previous comments on typical ranges, values of 1.45 and 2.59 were assumed for the tortuosity of oxide and salt, respectively. While the exact membrane working condition cannot be determined in the absence of measurements performed with the membrane under the same operating

Table 2
Survey of membrane characteristics used in Fig. 5.

Solid Oxide	J_{CO_2} (mL cm^{-2} min^{-1})	I_{exp} (A)	χ_{SO}	$\ln(pCO_{2,f}/pCO_{2,p})$	S (cm^2)	d (cm)	Ref.	I_{th} (A)
SDC	0.123	1.62×10^{-2}	0.5	5.03	0.921	0.132	[38]	2.13×10^{-2}
BYS	0.04957	1.21×10^{-2}	0.75	5.00	1.69	0.005	[4]	5.09
CGO	0.236	1.69×10^{-2}	0.73	4.44	0.5	0.092	[23]	2.54×10^{-2}

J_{CO_2}–flux of CO_2 across the membrane; I_{exp} – equivalent ionic current across the membrane; χ_{SO} – volume fraction of SO; I_{th} – estimated ionic current using eq. (10) and literature data listed in Table 1.

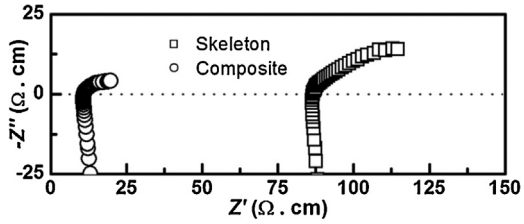

Fig. 6. Impedance spectroscopy results (corrected for the cell dimensions) obtained in air, at 923 K, with a CGO skeleton (73% densification) and a CGO + NLC composite similar to the membrane used in published CO_2 permeation experiments [23].

conditions, the coherence of the entire exercise means that the experimental ionic current through the CGO-based membrane can be easily explained using small and reasonable numbers for the tortuosity of both phases. Also, as mentioned, other authors published close results using one SDC-based membrane [38]. In all these circumstances surface/interface reaction kinetic constraints seem irrelevant.

In Fig. 5b the situation corresponding to the BYS-based membrane is entirely distinct. Firstly the gap between I_{th} and I_{exp} is enormous forcing the adoption of distinct current scales to see both conditions. The figure inset shows I_{th} while the larger diagram shows the region closer to I_{exp}. The large target value is due to the combination of a superior oxide-ion conductivity of BYS with respect to the other oxides together with a membrane thickness of only 0.005 cm obtained using a sophisticated processing route (Table 2). Both effects should boost the permeation current, according to equation (10).

To go deeper in the analysis of these results, several sets of tortuosity values are again considered in the larger diagram in Fig. 5b. The abnormal limiting values where the tortuosity of one single phase would explain the observed membrane current are $\tau_{MC} = 3190$ and $\tau_{SO} = 486$. Even considering tortuosity values in the order of 100 in both phases (lines c and c'), a sluggish surface/interface reaction kinetics would be need to account for the corresponding hypothetical voltage drop $V_{hyp.pol}$.

Published results on this membrane list several aspects that might account for the observed performance [4]. As example, the interface between BYS and the molten carbonates was covered with alumina particles to improve the wettability. A thin poorly conducting layer is likely to be formed between BYS and the molten carbonates as mandatory pathway for oxide-ion transport between BYS and the molten carbonates. Alumina is indeed known to react with the molten carbonates yielding namely $LiAlO_2$ [40]. This is a highly insulating phase with an electrical conductivity in the order of 5.1×10^{-5} S cm^{-1} at 923 K [41] and oxide ion-conductivity in this layer is presumably below this already low value. In the reaction schemes and equivalent circuits previously presented this would correspond to a new pair of resistors of unknown magnitude (R_3 and R_4) between cells (see Fig. 2c and d). When such resistors are crossed by the inner cell current they are obviously responsible for a voltage drop that might be significant, depending on the layer thickness and exact oxide-ion conductivity. Consistently with these comments, in the field of Solid Oxide Fuel Cells the presence of thin insulating layers between cathode and electrolyte are a known reason for serious degradation of surface reaction kinetics and large overvoltages [42].

3.4. Final remarks

The newly introduced diagram was clearly able to provide significant insight on membrane performance. In the case of ceria-based membranes with typical microstructures the performance might be improved namely decreasing estimated tortuosity factors (e.g., fully aligned pores within a ceramic matrix), but actual numbers are already small. Decreasing membrane thickness is probably the most effective design parameter that might be improved in this case.

For BYS and related compositions, due to the magnitude of the effects needed to account for the mismatch between actual and target performance, basic issues related to chemical stability are presumably nuclear in membrane design.

Although mostly discarded in the studied cases, slow surface/interface kinetics can be easily considered in the newly presented diagrams. In circumstances where reliable information is available on the ionic resistance of both phases, proper mapping of membrane performance is able to provide quantitative information on the role of surface/interface kinetics. This capability can be used to obtain further guidance on membrane design.

Final comments are also needed on the global assumptions behind the model and approach previously introduced. Firstly, the electronic conductivity of both phases, and the corresponding dependence on the gas phase composition were both neglected. As already mentioned, by definition the electronic conductivity of common solid electrolytes is quite small with respect to the ionic conductivity [43] unless we use extremely reducing conditions, unusual at least in post-combustion treatments. With respect to molten carbonates the uncertainty on electronic transport is higher but the fact that these electrolytes are used at 600–700 °C in MCFCs, without sign of deviation between ideal (open circuit thermodynamic) and effective cell voltages also points towards negligible electronic conductivity. In fact, the only reported attempt to measure the electronic conductivity of similar composite electrolytes suggests a negligible value, orders of magnitude below the reported ionic conductivity [11].

The ionic conductivity dependencies on the partial pressure of CO_2 and O_2 were also neglected. Again, in the case of ceramic oxide-ion conductors this seems to describe accurately the known characteristics of these materials [44]. In the case of molten carbonates the known gas phase concentration effects are modest at typical working temperatures even when moving between pure O_2 and pure CO_2 [45]. So, again, the approximation seems sensible.

4. Conclusions

Based on a classical equivalent circuit and ordinary assumptions on circuit elements, a simple approach can be used to obtain insight on relevant parameters determining the performance of

composite CO_2 separation membranes. A new illustrative diagram inspired in corrosion (Evans-type) plots provides a simple visual perspective on all these aspects. Handling of information on candidate constituent phases allows the gross selection of ideal phase compositions and working temperatures for improved membrane performance. Lastly, adequate mapping of reported CO_2 permeation data against ideal values showed that ceria-based membranes perform relatively better than their equivalents based on bismuth oxide, irrespective of the latter higher absolute values. Formation of interfacial insulating layers between oxide and salt, due to reaction between membrane constituents, or slow surface reactions can easily explain a significant drop in performance and should be considered in the selection of membrane materials.

Acknowledgement

Funding from FEDER/COMPETE and FCT (Portugal) via Project NANOMFC (New-INDIGO/0001/2013), and from Project CICECO-Aveiro Institute of Materials (Ref. FCT UID/CTM/50011/2013), financed by national funds through FCT/MEC and when appropriate co-financed by FEDER under the PT2020 Partnership Agreement is greatly appreciated. S. Patrício thanks FCT for the postdoctoral grant (SFRH/BPD/75943/2011) and F. Marques thanks CNPq (Brazil) for the grant PVE 401174/2012-3 as Special Invited Researcher at IPEN, S. Paulo.

References

[1] K. Pointon, B. Lakeman, J. Irvine, J. Bradley, S. Jain, The development of a carbon–air semi fuel ce-ll, J. Power Sources 162 (2006) 750–756.
[2] B. Zhu, X. Liu, P. Zhou, X. Yang, Z. Zhu, W. Zhu, Innovative solid carbonate –ceria composite electrolyte fuel cells, Electrochem. Comm. 3 (2001) 566–571.
[3] Y. Li, Z. Rui, C. Xia, M. Anderson, Y.S. Lin, Performance of ionic-conducting ceramic/carbonate composite material as solid oxide fuel cell electrolyte and CO_2 permeation membrane, Catal. Today 148 (2009) 303–309.
[4] Z. Rui, M. Anderson, Y. Li, Y.S. Lin, Ionic conducting ceramic and carbonate dual-phase membranes for carbon dioxide separation, J. Membr. Sci 417–418 (2012) 174–182.
[5] X. Dong, J.O. Landeros, Y.S. Lin, An asymmetric tubular ceramic-carbonate dual phase membrane for high temperature CO_2 separation, Chem. Commun. 49 (2013) 9654–9656.
[6] B. Zhu, I. Albinsson, C. Andersson, K. Borsand, M. Nilsson, B.-E. Mellander, Electrolysis studies based on ceria-based composites, Electrochem Commun 8 (2006) 495–498.
[7] I.A. Amar, C.T.G. Petit, L. Zhang, R. Lan, P.J. Skabara, S. Tao, Electrochemical synthesis of ammonia based on doped-ceria-carbonate composite electrolyte and perovskite cathode, Solid State Ionics 201 (2011) 94–100.
[8] R.L. Frederick, E.K. Williams, ^{23}Na and ^{14}C Diffusion in a Mixture of Li/Na/KCO_3, J. Electrochem. Soc. 116 (1969) 454–455.
[9] P.L. Spedding, R. Mills, Trace-Ion Diffusion in Molten Alkali Carbonates, J. Electrochem. Soc. 112 (1965) 594–599.
[10] P.L. Spedding, R. Mills, Tracer Diffusion Measurements in Mixtures of Molten Alkali Carbonates, J. Electrochem. Soc. 113 (1966) 599–603.
[11] W. Zhu, C. Xia, D. Ding, X. Shi, G. Meng, Electrical properties of ceria-carbonate composite electrolytes, Mater. Res. Bull. 41 (2006) 2057–2064.
[12] A. Evans, W. Xing, T. Norby, Electromotive Force (emf) Determination of Transport Numbers for Native and Foreign Ions in Molten Alkali Metal Carbonates, J. Electrochem. Soc. 162 (2015) F1135–F1143.
[13] H. Näfe, Electrochemical CO_2 Separation through an Alkali-Carbonate-Based Membrane, ECS J. Solid State Sci. Technol. 3 (2014) N23–N29.
[14] S.H. White, U.M. Twardoch, The Electrochemical Behaviour of Solutions of Molten Ternary Alkali Carbonate Mixture Equilibrated with Carbon Dioxide-Water Mixtures at 460 °C, Electrochim. Acta 29 (1984) 349–359.
[15] X. Wang, Y. Ma, S. Li, A.-H. Kashyout, B. Zhu, M. Muhammed, Ceria-based nanocomposite with simultaneous proton and oxygen ion conductivity for low-temperature solid oxide fuel cells, J. Power Sources 196 (2011) 2754–2758.
[16] Y. Zhao, C. Xia, Y. Wang, Z. Xu, Y. Li, Quantifying multi-ionic conduction through doped ceria-carbonate composite electrolyte by a current-interruption technique and product analysis, Int. J. Hydrogen Energ. 3 (2012) 8556–8561.
[17] A.S.V. Ferreira, C.M.C. Soares, F.M.H.L.R. Figueiredo, F.M.B. Marques, Intrinsic and extrinsic compositional effects in ceria/carbonate composite electrolytes for fuel cells, Int. J. Hydrogen Energ. 36 (2011) 3704–3711.
[18] S. Scaccia, S. Frangini, Oxygen dissolution behaviour in (52/48) mol% Li_2CO_3/Na_2CO_3 electrolyte containing Ba and Ca additives, J. Mol. Liq. 129 (2006) 133–137.
[19] L.-J. Chen, C.-J. Lin, J. Zuo, L.-C. Song, C.M. Huang, First spectroscopic observation of peroxocarbonate/peroxodicarbonate in molten carbonate, J. Phys. Chem. B 108 (2004) 7553–7556.
[20] K.-P. Zeller, P. Schuler, P. Haiss, The hidden equilibrium in aqueous sodium carbonate solutions- evidence for the formation of the dicarbonate anion, Eur. J. Inorg. Chem. 16 (2005) 168–172.
[21] P. Claes, D. Moyaux, D. Peeters, Solubility and solvation of carbon dioxide in the molten Li_2CO_3/Na_2CO_3/K_2CO_3 (43.5:31.5:25.0 mol-%) eutectic mixture at 973 K I. Experimental part, Eur. J. Inorg. Chem. 3 (1999) 583–588.
[22] Y. Gong, X. Li, L. Zhang, W. Tharp, C. Qin, K. Huang, Molten carbonates as an effective oxygen reduction catalyst for 550–650 °C Solid Oxide Fuel Cells, J. Electrochem. Soc. 160 (2013) F958–F964.
[23] S.G. Patrício, E. Papaioannou, G. Zhang, I.S. Metcalfe, F.M.B. Marques, High performance composite CO_2 separation membranes, J. Membr. Sci. 471 (2014) 211–218.
[24] M. Mogensen, N.M. Sammes, G.A. Tompsett, Physical, chemical and electrochemical properties of pure and doped ceria, Solid State Ionics 129 (2000) 63–94.
[25] B.C.H. Steele, Appraisal of $Ce_{1-\gamma}Gd_{\gamma}O_{2-\gamma/2}$ electrolytes for IT-SOFC operation at 500 °C, Solid State Ionics 129 (2000) 95–110.
[26] T. Kojima, Y. Miyazaki, K. Nomura, K. Tanimoto, Electrical conductivity of molten Li_2CO_3-X_2CO_3 (X: Na, K, Rb, and Cs) and Na_2CO_3-Z_2CO_3 (Z: K, Rb, and Cs), J. Electrochem. Soc. 154 (2007) F222–F230.
[27] P.L. Spedding, Electrical Conductance of Molten Alkali Carbonate Binary-Mixtures, J. Electrochem. Soc. 120 (1973) 1049–1052.
[28] J.L. Wade, K.S. Lackner, A.C. West, Transport model for high temperature, mixed conducting CO_2 separation membranes, Solid State Ionics 178 (2007) 1530–1540.
[29] Z. Rui, M. Anderson, Y.S. Lin, Y. Li, Modeling and analysis of carbon dioxide permeation through ceramic-carbonate dual-phase membranes, J. Memb. Sci. 345 (2009) 110–118.
[30] J. Ortiz-Landeros, T. Norton, Y.S. Lin, Effects of support pore structure on carbon dioxide permeation of ceramic-carbonate dual-phase membranes, Chem. Eng. Sci. 104 (2013) 891–898.
[31] T.P. Hoar, L.E. Price, The electrochemical interpretation of Wagner's theory of tarnishing reactions, Trans. Faraday Soc. 34 (1938) 867b–872.
[32] C. Wagner, Theory of the tarnishing process, Z. Phys. Chem. B 21 (1933) 25–41.
[33] J.W. Patterson, Ionic and Electronic Conduction in Nonmetallic Phases, Corrosion Chemistry 4 (1979) 96–125.
[34] R.M.C. Marques, F.M.B. Marques, J.R. Frade, Characterization of Mixed Conductors by DC Techniques. Part I: Theoretical Solutions, Solid State Ionics 73 (1994) 15–25.
[35] W.H. Hayt, J.E. Kemmerly, Engineering Circuit Analysis, 2nd ed., Book Company Inc., McGraw-Hill, 1971, pp. p.35.
[36] D.W. Strickler, W.G. Carlson, Electrical conductivity in the ZrO_2-rich region of several M_2O_3-ZrO_2 systems, J. Am. Ceram. Soc. 48 (1965) 286–289.
[37] Y. Zeng, Y.S. Lin, Synthesis and properties of copper and samarium doped yttria-bismuth oxide powders and membranes, J. Mat. Sci. 36 (2001) 1271–1276.
[38] J. Tong, L. Zhang, M. Han, K. Huang, Electrochemical separation of CO_2 from a simulated flue gas with high-temperature ceramic–carbonate membrane: New observations, J. Membr. Sci. 477 (2015) 1–6.
[39] D. Pérez-Coll, E. Sánchez-López, Glenn C. Mather, Influence of porosity on the bulk and grain-boundary electrical properties of Gd-doped ceria, Solid State Ionics 181 (2010) 1033–1042.
[40] A.S.V. Ferreira, T. Saradha, F.L. Figueiredo, F.M.B. Marques, Compositional and microstructural effects in composite electrolytes for fuel cells, Int. J. Energ. Res. 35 (2011) 1090–1099.
[41] A.I.B. Rondão, N.C.T. Martins, S.G. Patrício, F.M.B. Marques, Ionic transport in (nano)composites for fuel cells, Int. J. Hydrogen Energ. 41 (2016) 7666–7675.
[42] A. Mitterdorfer, L.J. Gauckler, $La_2Zr_2O_7$ formation and oxygen reduction kinetics of the $La_{0.85}Sr_{0.15}Mn_yO_3$, O_2(g)|YSZ system, Solid State Ionics 111 (1998) 185–218.
[43] V.V. Kharton, F.M.B. Marques, A. Atkinson, Transport Properties of Solid Oxide Electrolyte Ceramics: a Brief Review, Solid State Ionics 174 (2004) 135–149.
[44] F.M.L. Figueiredo, F.M.B. Marques, Electrolytes for solid oxide fuel cells, WIREs Energy Environ. 2 (2013) 52–72.
[45] A.I.B. Rondão, S.G. Patrício, F.M.L. Figueiredo, F.M.B. Marques, Role of gas-phase composition on the performance of ceria-based composite electrolytes, Int. J. Hydrogen Energ. 38 (2013) 5497–5506.